Physical controls of dynamics of methane venting from a shallow seep area west of Svalbard

A. Silyakova[1], P. Jansson[1], P. Serov[1], B. Ferré[1], A. K. Pavlov[2], T. Hattermann[3,4], C. A. Graves[5,6], S. M. Platt[7], C. Lund Myhre[7], F. Gründger[1] and H. Niemann[8,1,9]

[1]CAGE-Centre for Arctic Gas Hydrate, Environment and Climate, UiT the Arctic University of Norway in Tromsø, Department of Geosciences, Tromsø, Norway
[2]Norwegian Polar Institute, Fram Centre, Tromsø, Norway
[3]Akvaplan-niva AS, Fram Centre, Tromsø, Norway
[4]Alfred Wegener Institute, Helmholtz Centre for Polar and Marine Research, Bremerhaven, Germany
[5]Leibniz Institute for Baltic Sea Research Warnemünde, Rostock, Germany
[6]Centre for Environment, Fisheries and Aquaculture Science, Lowestoft, UK
[7]NILU - Norwegian Institute for Air Research, Kjeller, Norway
[8]University of Basel, Basel, Switzerland
[9]NIOZ Royal Netherlands Institute for Sea Research, Department of Marine Microbiology & Biogeochemistry, the Netherlands

Corresponding author: Anna Silyakova (**anna.silyakova@uit.no**)

Key Points:

- Gas seepage intensity and lateral water mass movements are key controls of water column methane content
- Vertical methane transport is limited irrespective of stratification
- Eddies play a key role in horizontal advection and dispersion of dissolved methane

Abstract

We investigate methane seepage on the shallow shelf west of Svalbard during three consecutive years, using discrete sampling of the water column, echosounder-based gas flux estimates, water mass properties, and numerical dispersion modelling. The results reveal three distinct hydrographic conditions in spring and summer, showing that the methane content in the water column is controlled by a combination of free gas seepage intensity and lateral water mass movements, which disperse and displace dissolved methane horizontally away from the seeps. Horizontal dispersion and displacement of dissolved methane are promoted by eddies originating from the West Spitsbergen Current and passing over the shallow shelf, a process that is more intense in winter and spring than in the summer season. Most of the methane injected from seafloor seeps resides in the bottom layer even when the water column is well mixed, implying that the controlling effect of water column stratification on vertical methane transport is small. Only small concentrations of methane are found in surface waters, and thus the escape of methane into the atmosphere above the site of seepage is also small. The magnitude of the sea to air methane flux is controlled by wind speed, rather than by the concentration of dissolved methane in the surface ocean.

1 Introduction

The Arctic Ocean holds vast reservoirs of the powerful greenhouse gas methane in the form of free and dissolved gas (Lammers et al., 1995; Damm et al., 2005), gas entrapped in subsea permafrost (Shakhova et al., 2010), and gas hydrates in sediments (Hester and Brewer, 2009; Westbrook et al., 2009; Berndt et al., 2014). In particular, gas that is bound in hydrates may be released as a result of temperature induced gas hydrate destabilization (Kretschmer et al., 2015; James et al., 2016), which makes the warming Arctic Ocean a potential hot spot of future methane emission (Shakhova et al., 2010; Kort et al., 2012; Parmentier et al., 2015). Methane release from the seafloor has been documented from numerous areas along the Arctic Ocean continental margin: the West Spitsbergen continental margin and shelf (Knies et al., 2004; Damm et al., 2005; Westbrook et al, 2009; Sahling et al., 2014; Smith et al., 2014; Graves et al., 2015; Mau et al., 2017), the Barents Sea (Lammers et al., 1995; Serov et al., 2017; Andreassen et al., 2017), the Kara Sea shelf (Portnov et al., 2013; Serov et al., 2015), the East Siberian Shelf (Shakhova et al., 2010, 2013), and the Beaufort Sea (Kvenvolden et al., 1993; Paull et al., 2007). Methane release from the West Spitsbergen margin has been ongoing for several millennia and is, at least partly, temperature controlled (Berndt et al., 2014).

Indeed, Arctic air temperatures are increasing twice as fast as the global average because of Arctic amplification (Graversen et al., 2008; Serreze and Francis, 2006; IPCC 2014). The annual average Arctic air temperature is now 3.5°C warmer compared to the beginning of 20th century (Soreide et al., 2016). As a result, expanding areas of ice-free Arctic Ocean waters are being exposed to solar radiation and elevated air temperatures. Combined with an increase of heat input from adjacent ocean basins, e.g. warmer than usual Atlantic Water (AW) propagating deeper into the Arctic Ocean (Polyakov et al., 2004; 2007; 2010), this results in a present day Arctic Ocean sea surface temperature which is 5°C warmer than the 1982-2010 average for the Barents and Chukchi seas and around Greenland (Soreide et al., 2016). The effect of increasing temperature in the future Arctic may therefore become more important for Arctic seafloor methane liberation (Westbrook et al., 2009; Ferré et al., 2012; Marín Moreno et al., 2015).

Several processes determine the fate of methane released into the water column from sediments and, most importantly, its release to the atmosphere. Methane contained in bubbles emanating from the seafloor dissolves in seawater and can be rapidly transported from the area by the advection of water masses (Graves et al., 2015). The upward transport of dissolved methane has been found to be limited by water column stratification (e.g. Schmale et al., 2005; Leifer et al., 2009). Studies by Myhre et al., (2016) and Gentz et al., (2014) conducted on the shallow shelf and upper continental slope off Svalbard, west of Prins Karls Forland (PKF) revealed waters enriched with dissolved methane below the pycnocline. However, the methane concentrations above the pycnocline were generally in equilibrium with the atmospheric mixing ratio. This suggested that the pycnocline may act as a physical barrier, preventing dissolved methane from entering the well-mixed upper layer of the water column and thus also the atmosphere, instead trapping methane in the lower sphere of the water column. The open Arctic Ocean is stratified throughout the year (Rudels et al., 1994). In shallower areas, however, the stratification of the entire water column is subject to an annual cycle and a seasonal erosion of the pycnocline e.g. through winter time convection or wind induced mixing (Cottier et al., 2010). If controlled by stratification, the escape of methane to the atmosphere would also follow this seasonality. In other words, the potential for methane to be liberated to the atmosphere

from these areas is higher when there is no stratification during stormy seasons (von Deimling et al., 2011).

Another important process determining the fate of methane in the water column is its removal by aerobic methane oxidation (MOx), mediated by aerobic methanotrophic bacteria (Hanson & Hanson, 1996; Reeburg, 2007; Steinle et al., 2015). Methane removal from deep-water sources through MOx is more efficient than that from shallow sources, because the distance between methane liberation from the seafloor and potential methane evasion to the atmosphere is greater and methanotrophs in the water column have more time for methane consumption (Steinle et al., 2015; Graves et al., 2015; James et al., 2016). For example, in the deep Gulf of Mexico (~1500 meters water depth), most of the methane discharged following the Deepwater Horizon oil spill was consumed by water column methanotrophs (Kessler et al., 2011), while most of methane seeping from the shallow seafloor on the East-Siberian Shelf (~50 m water depth) was liberated to the atmosphere, especially during storm-induced mixing events (Shakhova et al., 2013).

Marine environments in the Arctic Ocean characterized by ongoing methane release are ideal natural laboratories for studying the effects of potentially enhanced seafloor methane venting in warming waters, and the processes that regulate the transport of this methane. In this paper, we study the dynamics of methane venting from shallow gas-bearing sediments (water depth: 50-120 meters) west of PKF off the Svalbard archipelago; and the physical processes in the water column that control methane dispersion and displacement away from the seeps. We conducted oceanographic surveys to determine the flux of free gas (i.e. bubbled methane) from sediments, concentrations of dissolved methane in the water column, sea-air methane fluxes, and water mass properties. Measurements were repeated in a defined study area during three consecutive years to investigate the dynamics of venting methane under varying hydrographic conditions. Model simulations place these detailed observations into the broader seasonal context, and allow a better understanding of the oceanographic processes controlling methane dynamics in the area of study.

The paper is structured as follows: Section 2 provides an overview of the study region and summarizes the different datasets and methods used in the analysis. Section 3 presents the results and successively examines the controls of the methane fluxes from the sediment (sources), the controls of the sea-air methane fluxes (sink I), the controls of the methane content in the water column (sink II), the controls of the vertical distribution of the dissolved methane, and the controls of the horizontal distribution of the dissolved methane. Section 4 discusses the implications of main findings on the controls of the methane distribution and provides the conclusions of the paper

2 Methods

2.1 Study area

Our study area (423 km^2; 50 - 120 m water depth) is located west of PKF (Fig. 1). The seafloor in this area is complex and characterized by abundant depressions and a sequence of pronounced end moraine ridges: the Forlandet moraine complex (Landvik et al., 2005). Several hundred methane flares were found during the present study and previous expeditions (e.g. Sahling et al., 2014 and references therein). Similar to the adjacent shelf break, gas seepage is not related to pockmarks or other fluid leakage related structures and the origin of the methane remains unconfirmed (Westbrook et al., 2009; Berndt et al., 2014). Although hydrates have never been recovered in the area and seismic evidence of

gas hydrates is missing, sediment cores drilled outside PKF contained freshwater presumably originating from dissociated gas hydrates (Wallmann et al., 2018). Previous studies also suggest that free gas may originate from gas hydrate dissociation deeper on the continental slope (>300 m) where gas hydrates have been found (Sarkar et al., 2012) and migrate along the permeable zones towards the shelf (Westbrook et al., 2009). An alternate hypothesis is that glacial rebound at the beginning of the Holocene resulted in gas hydrate dissociation, which allowed for the formation of shallow gas pockets that continue to release methane into the water column (Portnov et al., 2016; Wallmann et al., 2018).

The water masses and circulation in the study area are controlled to a large extent by the interaction of coastal processes on the shelf with the West-Spitsbergen Current (WSC) that circulates northward along the shelf break as the northernmost extension of the North-Atlantic Current, transporting AW into the Arctic Ocean. The core of the WSC is at 250-800 meters water depth (Perkin and Lewis, 1984) and the stream follows the slope of the continental margin (Aagaard et al., 1987). By bringing large amounts of salt and heat, it affects the water column structure in the entire area. Other currents in the area are the East Spitsbergen Current (ESC) that advects Arctic waters into the region, and the coastal surface current, associated with the West Spitsbergen Polar Front (Nilsen et al., 2016). Local scale physical processes affecting water mass circulation include exchange of water masses between the WSC and shelf waters due to instability of the WSC core and resulting eddies (Teigen et al., 2010; Hattermann et al., 2016; Appen et al., 2016); as well as wind forcing and resulting upwelling events (Berge et al., 2005; Cottier et al., 2007).

2.2 Survey design

We conducted research expeditions with the R/V Helmer Hansen in the study area during three consecutive years: 25-27 June 2014 (hereafter, June-14), 01 – 03 July 2015 (July-15), 02 – 04 May 2016 (May-16). Each year we visited 64 hydrographic stations. Stations were positioned in a grid for comprehensive coverage of the water column above active methane seeps (Fig. 1). We collected hydrocast data from each station including continuous measurements of conductivity, temperature, depth (CTD), and sampled the water column at discrete depths for subsequent dissolved methane concentration measurements (see details in section 2.4). The entire grid was subsampled within 3 days during each survey. Underway hydro-acoustic scanning of the water column was performed to acquire information on gas flares (section 2.3). Ship-mounted meteorological instruments continuously recorded air temperature, atmospheric pressure, wind speed and direction. Furthermore, atmospheric methane mixing ratios were recorded continuously with a Cavity Ring-Down Spectrometer (CRDS, PICARRO G2401) with an air intake at 22.4 m above sea level.
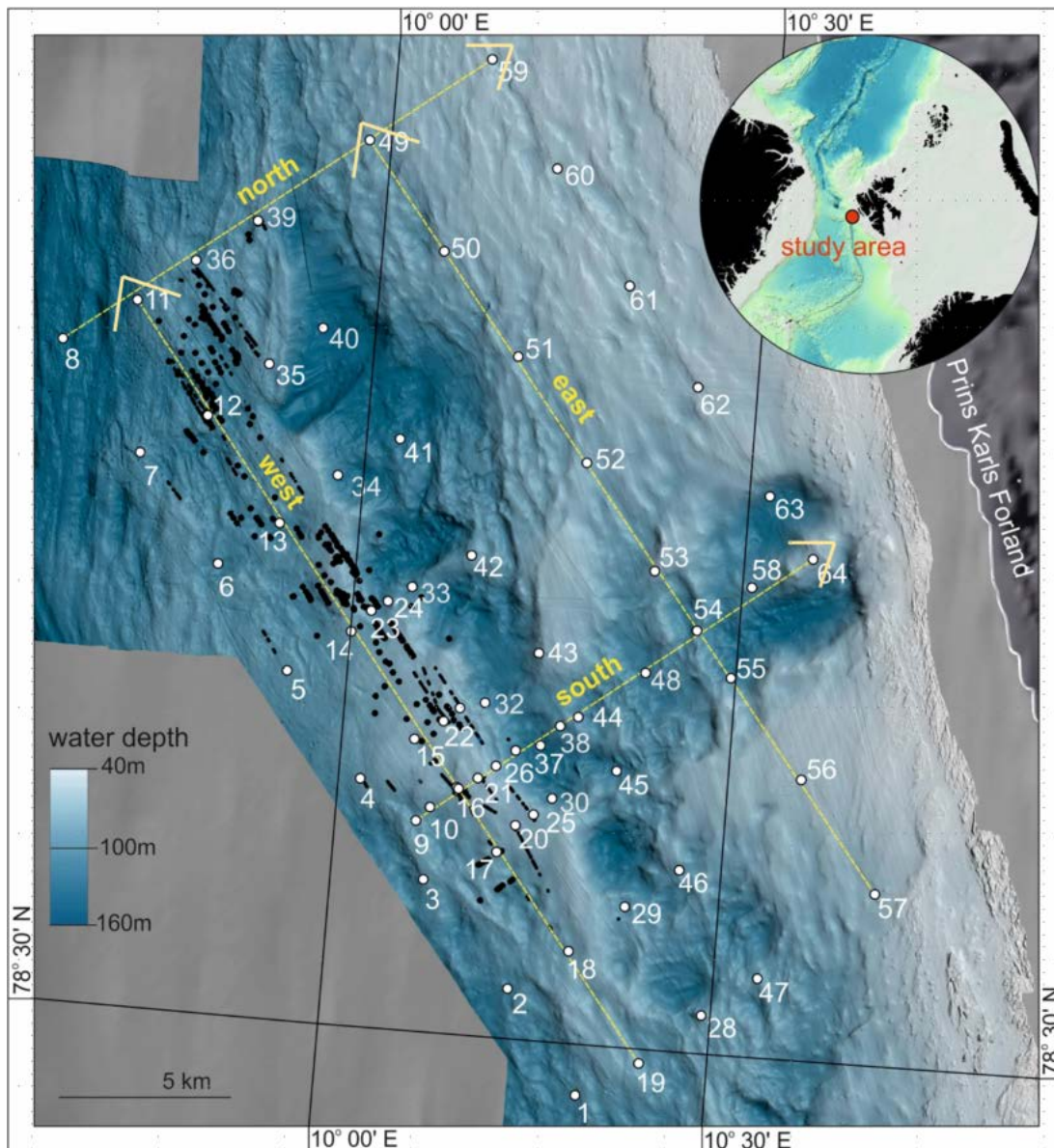
Figure 1. Bathymetric map of the study area with 64 hydrographic stations (white dots) for oceanographic measurements west of the Svalbard archipelago (overview map). Black dots indicate locations of methane seeps detected on echograms during all three surveys. Yellow dashed arrows indicate transects shown in Fig. 4. Bathymetry data were acquired on board with a Kongsberg Simrad EM 300 multibeam echo sounder (frequency of 30 kHz).

2.3 Hydroacoustic data acquisition and gas flux calculations

Gas bubbles in the water column were detected as acoustic signatures (flares) with a Kongsberg Simrad EK60 single beam echosounder system. This system is primarily designed for the fishery industry, but is also used to detect gas bubbles in the water column (Ostrovsky et al., 2008; Nikolovska et al., 2008). Data were acquired at 38 kHz as this is the most appropriate frequency to detect gas bubbles of sizes expected for cold seeps (Greinert et al., 2006). We used the FlareHunter program (Veloso et al., 2015) to distinguish flares from other echo signals such as fish, seafloor, and interference artifacts, and calculated flow rates from echosounder backscatter based on beam compensated Target Strength (TS, dB) in a 5-10 meter layer above the seafloor. We report free gas

flow rates as mean values calculated from seven different bubble rising peed models (BRSMs). The relative uncertainty between BRSM estimates is 16 % (Veloso et al., 2015). The total length of our survey line was 408 km in June-14, 427 km in July-15, and 300 km in May-16. Accounting for water depth and the resulting beam width radii of 5 – 20 m, the area of the seafloor investigated by the echosounder was 5.5 km^2 in June-14 and July-15, and 3.8 km^2 in May-16, which amounts to ~1 % of the total study area. Since the fraction of the study area covered by echosounder was small and slightly different between the three surveys, we applied Kriging interpolation to scale up estimates over the entire study area and thus facilitate comparison (details are provided in supporting information Text S1 and Fig. S1). Note that Fig. 2 shows observed flow rates of single sources. For comparison with other studies we present flow rates for the whole study area in Table 2 calculated as: (i) integrated over the entire area volumetric flow rate (L min^{-1}); (ii) converted into mass flow rate (t y^{-1}) using the ideal gas law and accounting for the average depth within each cell; and (iii) mean flux averaged over the whole area (mmol m^{-2} d^{-1}), converted from mass flow rate using the molecular weight of methane and divided by the survey area (423 km^2).

2.3 CTD profiling and water sample analyses

Vertical profiles of seawater temperature, salinity and pressure were recorded with a SBE 911 plus CTD probe at a rate of 24 Hz. The probe was mounted on a rosette including 12 5-litre Niskin bottles. The Niskin bottles were closed during the up-cast (at speed of 1 m s^{-1}). For analysis of hydrographic profiles, only down-casts were considered. Water samples were taken at 5, 15 and 25 meters above the seafloor and below the sea surface, and an additional two samples were collected at evenly spaced depth levels between 25 m above the seafloor an 25 m below the sea surface. In total, eight depths were sampled during all surveys.

Immediately upon recovery, sub-samples from the Niskin bottles were collected through silicon tubing into 60 ml plastic syringes (June-14) or 120 ml serum glass bottles (Jule-15, May-16) with rinsing by 2 – 3 overflow volumes. Syringes were closed with a 2-way valve and serum bottles were crimp-sealed with butyl rubber septa. 5 ml N_2 headspace was added to the syringes and serum bottles. Syringes/serum bottles with headspace were vigorously shaken for two minutes to allow the headspace N_2 to equilibrate with the dissolved methane in the water sample. Headspace methane mixing ratios were determined by gas chromatography (GC). During the June-14 survey a ThermoScientific FOCUS GC equipped with a flame ionization detector (FID), and a Resteck 2 m packed column HS-Q 80/100 with hydrogen (40 ml min) as a carrier gas was used. During the July-15 and May-16 surveys a ThermoScientific Trace 1310 GC equipped with an FID, and a Restek 30 m Alumina BOND/Na_2SO_4 column with hydrogen as a carrier gas (40 ml min^{-1}) was used. The column temperature was held constant at 40°C. The systems were calibrated with external standards (2 ppm and 30 ppm in June-14 (Air Liquide); 10 ppm, 50 ppm, and 100 ppm in July-15 and May-16 (Carbagas). Finally, water column methane concentrations were calculated from headspace methane mixing ratios according to Wiesenburg & Guinasso (1979) with consideration of salinity, sample temperature and ambient atmospheric pressure.

2.4 Calculations of water column methane content

To account for the uneven bathymetry (bottom depths of 50 to 120 m), when comparing bottom, intermediate and surface waters, we divide the water column in three layers (Fig. S2): (1) a bottom layer (0-15 meters above seafloor), (2) an intermediate layer (15 meters above seafloor to 20 m water depth; the upper boundary roughly follows the depth of the pycnocline during the July-15 survey,

which we determined as a function of the Brunt–Väisälä frequency, see Fig. 5) and (3) a surface layer (20 m water depth to sea surface). Detailed calculations of the methane content (in mol) within the study area can be found in supporting information Text S2.

2.5 Calculations of the sea-air methane flux

The sea-air methane flux F (mol m^{-2} s^{-1}) was calculated according to Wanninkhof et al. (2009):

$$F = k(Cw - Co), \text{ (Eq. 1)}$$

where k is the gas transfer velocity (m s^{-1}), Co is the methane concentration (mol m^{-3}) at the ocean surface in presumed equilibrium with the atmosphere and Cw is the measured concentration of methane (mol m^{-3}) in the well-mixed surface layer, typically measured at 5 m water depth. The flux is positive and the ocean emits methane into the atmosphere if the measured concentration in the surface layer is greater than the equilibrium concentration. Co (mol m^{-3}) is defined as:

$$Co = \beta \, pCH_4, \text{ (Eq. 2)}$$

where β is the Bunsen solubility (mol m^{-3} atm^{-1}) of methane in seawater (Wiesenburg and Guinasso, 1979):

$$\beta = \exp[-68.8862 + 101.4956\left(\frac{100}{T_w}\right) + 28.7314\left[\ln\left(\frac{T_w}{100}\right)\right] + S(-0.076146 + 0.04397\left(\frac{T_w}{100}\right) - 0.0068672\left(\frac{T_w}{100}\right)^2], \text{ (Eq. 3)}$$

where Tw is the water temperature (K) and S is the salinity.

pCH_4 is the partial pressure of methane in the air, derived from the mixing ratio of methane in the atmosphere xCH_4 (mol mol^{-1}) measured by the on board CRDS at a height of 22.4 m (1902 ppb in June-14, 1917 ppb in July-15 and 1955 ppb in May-16). The pCH_4 was calculated according to Pierrot et al., (2009):

$$pCH_4 = xCH_4 * [P_{atm} - P_{wvapor}], \text{ (Eq. 4)}$$

accounting for the atmospheric pressure P_{atm} (atm) measured by the meteorological station on board, and the water vapor pressure P_{wvapor} (atm) calculated according to Weiss and Price (1980):

$$P_{wvapor} = exp[24.4543 - 67.4509\left(\frac{100}{T_A}\right) - 4.8489\ln\left(\frac{T_A}{100}\right) - 0.000544S], \text{ (Eq. 5)}$$

where T_A is the air temperature (K) from the ships' meteorological station and S is the salinity of spray in overlaying atmosphere, here assumed equal to the salinity of surface water.

The gas transfer velocity k is wind dependent and calculated as described in Graves et al. (2015) and references therein:

$$k = 0.24 * u_{10}^2 \left(\frac{Sc}{660}\right)^{-0.5}, \text{ (Eq. 6)}$$

where u_{10} (m s^{-1}) is the wind speed at 10 m above the sea surface, recalculated from the wind speed u_{meas} (m s^{-1}) measured by the ships' anemometer at height 22.4 m (z_{meas}) after Hsu et al., 1994:

$$u_{10} = u_{meas} * \left(\frac{Z_{meas}}{10}\right)^{-0.11}, \text{ (Eq. 7)}$$

The Schmidt number Sc in Eq. 6 is the non-dimensional ratio of gas diffusivity and water kinematic viscosity, and was defined as 677 in accordance with Wanninkhof et al., (2009).

2.6 Modelling of water mass properties and particle release experiments

To study seasonal variations in water mass properties and circulation and to scale up our observations to a full year, we used a high-resolution regional ocean sea ice model. A more detailed description and validation of the Svalbard 800 m horizontal resolution model (the S800-model hereafter) can be found elsewhere (Albretsen et al., 2017; Hattermann et al., 2016; Crews et al., 2017). Briefly, the S800-model provides hindcast ocean sea ice simulations for the Svalbard and the Fram Strait region based on the Regional Ocean Modelling System (ROMS, Shchepetkin and McWilliams, 2005) and a coupled sea ice component (Budgell, 2005). Boundary conditions are provided by a 4 km pan-Arctic setup (A4-model). Bathymetry is based on the ETOPO1 topography (Amante, 2009). Vertically, the model is discretized into 35 levels with a layer thickness of less than 1 m near the surface over the continental shelf. The S800-model is initialized and forced with daily averages from the A4-model, for which boundary conditions and forcing fields are based on reanalyses (Storkey et al., 2010). Atmospheric forcing is provided by ERA-interim reanalysis (Dee et al., 2011) and climatological river input from major rives in the area, including freshwater runoff from the Svalbard archipelago (details in Hattermann et al., 2016). The S800-model was initialized from January 2005, and the data shown in this study are based on model runs from July 2005 to July 2010, averaged every month over that period.

Modelling results were extracted from a modelled field that included 41×56 grid points and corresponded to the geographic area of the survey between CTD stations 1, 8, 57, 59, 64 (Fig.1; also red polygons in Fig. 10).

To investigate seasonal features of methane dispersion and displacement in the study area, we conducted numerical experiments by simulative release of neutrally buoyant Lagrangian drifters (hereafter particles) that were advected by the model velocity field. We released particles from the polygon where the most intense seeps were observed during the surveys. The polygon enclosed CTD stations 3 (113 m water depth), 4 (103 m water depth), 15 (91 m water depth), and 17 (97 m water depth) (Fig. 1). Due to varying water depths at these stations, we chose to release particles from uniform depths between 80 and 100 m. Trajectories were computed using Lagrangian particle tracking algorithm TRACMASS (Döös et al. 2017) based on the daily S800-model output (see Hattermann et al. 2016 for details). Particles were released every day and were tracked for a maximum lifetime of ten days. From the end positions of all particles released within a respective month, histograms of particle distributions were computed by bin-counting particle positions on the S800-model lattice. The histograms were normalized to the total number of particles and used as a proxy for mapping the particle dispersion in the region. In addition, monthly averages were computed according to the distance of particles from their source (as a measure of the particle displacement) and to the distance from their mean position at t = 5 days (particle dispersion).

3 Results and discussion

3.1 Controls on flare abundance and methane flux from sediments

We observed the densest flare cluster in the western and northwestern part of the study area (Fig. 2). This cluster was venting free gas during all cruises. In contrast, there was a difference in flare density between surveys in the southern part of the study area, with the highest flare density during the June-14 survey, and much lower densities during the July-15 and May-16 surveys. In total, we counted 225

individual flares in June-14, 208 in July-15 and only 92 during the May-16 survey. The estimated gas flux from individual flares ranged between 20 and 600 ml min^{-1} (Fig. 2). As a consequence of the decreasing flare density from June-14 to May-16, the calculated total volumetric gas flow rate over the surveyed area was larger for June-14 (900 L min^{-1}) than for the July-15 (665 L min^{-1}) and May-16 surveys (540 L min^{-1}) (Table 1).

We carefully checked for factors that may have potentially biased our estimates. The May-16 survey was substantially shorter in distance (~70% compared to June-14 and July-15), decreasing the confidence in scaling up our observations to the entire area. Yet, the western part of the study area, where we always observed the highest flare density, was investigated during all three surveys. Considering only this area, we could still identify a substantial decrease in both flare density and volume flux. Consequently, artefacts from the scaling up the observations made during surveys of different distance cannot explain the observed differences in seepage activity.

Temporal variability in the activity of seafloor methane seeps has been reported previously (e.g. Greinert et al., 2006; Klaucke et al., 2010; Kannberg et al., 2013). Römer et al. (2016) investigated a cold seep offshore Canada at 1250 m water depth and suggested that the pressure change of 1.9 dbar between low and high tide affected seepage activity with increasing gas flux during falling tides. However, our survey time period lasted for ~3 days, i.e. ~6 tidal cycles, so that potential forcing by tides should be equalized and tides cannot be the reason for differences in seepage activity between the surveys.

Variability in gas flux in our study area (highest in June-14, lower in July-15 and lowest in May-16) follows observed between-survey differences in bottom water temperature (Fig. S3). This was highest in June-14 (3.63±0.2°C), lower in July-15 (3.49±0.2°C) and the lowest in May-16 (1.77±0.1 °C). Indeed, it has been proposed that seasonal fluctuations in bottom water temperature modulate seepage activity off Svalbard, but from gas hydrate bearing sediments at the termination of the gas hydrate stability zone (Berndt et al., 2014). However, gas hydrates have never been found in our study area, which is at ~200 m shallower water depth than that of gas hydrate stability limit (>300 m water depth), so that we can only speculate about the mechanisms of a potential temperature control on seepage activity. Nevertheless, potentially modulating effects of bottom water temperature would imply seasonal fluctuations in seepage activity in our study area.
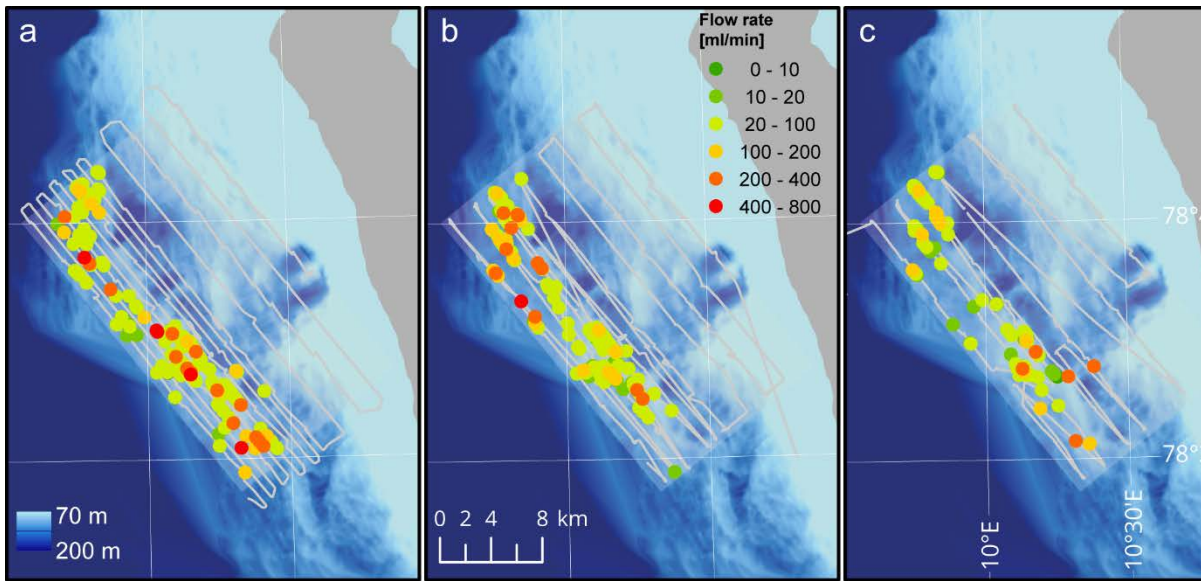
Figure 2. Flow rates from single sources (flares) during June-14 (**a**), July-15 (**b**) and May-16 (**c**) surveys. Coloured circles indicate gas flow rates in ml min^{-1} from individual flares on the seafloor. The grey line represents the ship track and echosounder beam coverage.

Table 1. Methane fluxes from sediments in different surveys

Survey	Total volumetric flow rate in the area (L min^{-1})	Total mass flow rate in the area (t y^{-1})	Average methane flux from sediments (mmol m^{-2} d^{-1})
June-14	899	3774	1.53
July-15	665	3004	1.21
May-16	542	2356	0.96

3.2 Controls of sea-air methane flux

The highest sea-air methane flux of 15 µmol m^2 d^{-1} was observed during the June-14 survey, a lower flux of 11 µmol m^2 d^{-1} was observed in July-15, and the lowest flux of only 2 µmol m^2 d^{-1} was observed during the May-16 survey (Fig. 3 d-f). The temporal pattern of atmospheric methane mixing ratios was the opposite of that of the flux, i.e. we found the lowest mixing ratios in June-14 (1902 ± 0.52 ppb), higher during the July-15 (1917 ± 3.30 ppb) and the highest during the May-16 survey (1955 ± 25.4 ppb) (data given as average ± standard deviation of all observations during each survey). Thus, the atmospheric mixing ratio of methane was one of the main controls on sea-air fluxes resulting in a suppressed flux in case of higher atmospheric methane values (e.g. lower fluxes in May-16 compared to the highest encountered atmospheric methane mixing ratios). A further key control on sea-air methane fluxes is the concentration of methane in the well-mixed surface waters, which was 9 nmol L^{-1} in June-14, and 3 nmol L^{-1} during the July-15 and May-16 surveys (Table 2). Despite the similar surface water concentrations in July-15 and May-16, sea-air methane fluxes were 5 times higher in July-15 than in May-16. This can be explained by the wind speed, which was comparably low and varied very little during the June-14 (4-8 m s^{-1}) and May-16 surveys (1-6 m s^{-1}), but increased from calm 4-6 m s^{-1} to strong 10-12 m s^{-1} towards the end of the 3-day July-15 survey (Fig. 3b). Generally, the differences between the atmospheric methane mixing ratio and surface water methane content as well as wind speed determine the variation in average sea-air flux. However, we argue that wind speed plays the most important role in our study area with respect to sea-air methane fluxes. High wind speeds can intensify efflux to the atmosphere even if the surface water methane concentration is relatively low as long as the surface waters are supersaturated with respect to the atmosphere.

To further test how the wind speed affects sea-air methane flux, we determined what the flux would have been if the wind speed had been a 5 m s^{-1} throughout all surveys. In other words, we used the observed values of surface water methane concentrations and atmospheric methane mixing ratios measured during each survey, but instead of the measured wind data, we calculated fluxes for a constant wind speed of 5 m s^{-1}, which is the climatological average wind speed for late spring to early summer in our study area (The Norwegian Meteorological Institute, www.yr.no). The meteorological mean was lower than the measured wind speed in June-14 and July-15, but higher than the measured wind speed in May-16. Therefore, our flux calculations with the mean values produced lower flux values for the June-14 (10 µmol m^2 d^{-1}) and July-15 (4 µmol m^2 d^{-1}) surveys, but higher values for the May-16 (3.5 µmol m^2 d^{-1}) survey (Fig. 3 g-i). This comparison between sea-air methane flux with

actual measured and constant wind speeds highlights the importance of wind speed in modifying methane emission to the atmosphere in our study area.
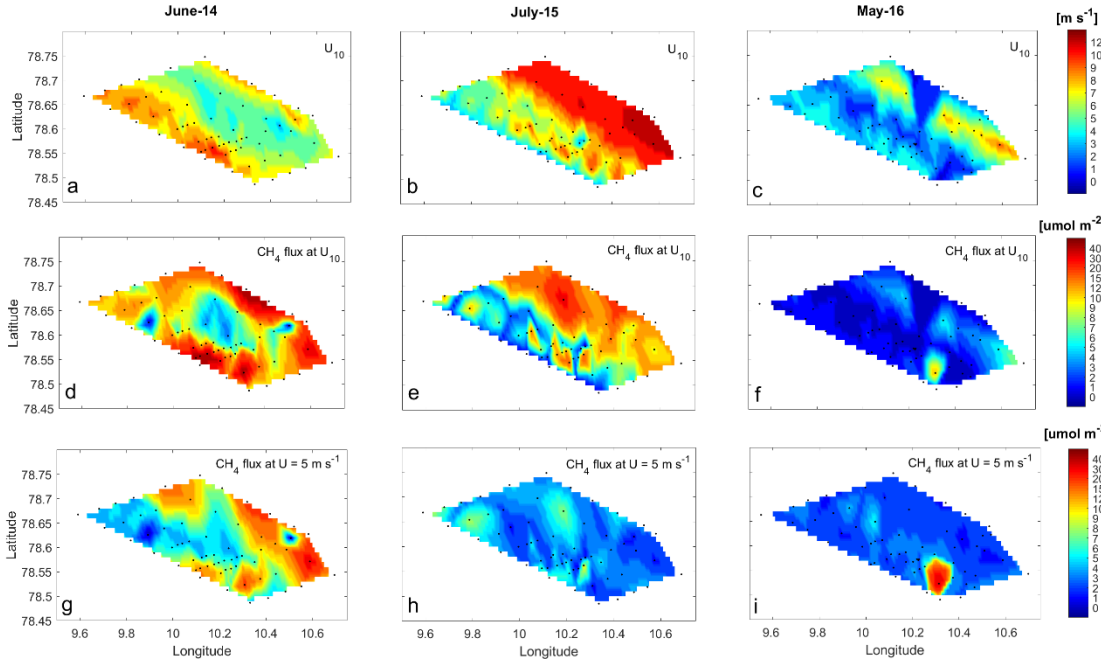

Figure 3. Wind speed measured at 22.4 m above sea level (upper panel: **a**, **b**, **c**), Methane flux at the air-sea interface at measured wind speed u_{10} (mid panel: **d**, **e**, **f**) and methane flux at the air-sea interface at constant wind speed U=5 m s^{-1} for May-July (lower panel: **g**, **h**, **i**), for the entire grid and the three surveys.

3.3 Controls of water column methane content

The water column above active methane flares in the study area was divided into three layers in order to estimate differences between methane content in the bottom 15 m, where presumably most of released methane dissolves; the surface 20 m which roughly corresponds to the thickness of the well mixed surface layer in summer and from which outgassing most of methane to the atmosphere occurs; and the intermediate layer between the bottom and surface layers, which is the thickest and presumably accumulates most of the released methane. When comparing different layers, the highest methane concentrations were found in bottom layer as expected. However, in all surveys the overall highest methane content was found in the intermediate layer because it contains the highest volume of water (extends through the largest depth interval). When comparing different surveys, we observed the highest total methane content in June-14 (23×10^5 mol), lower in July-15 (15×10^5 mol) and lowest during the May-16 (14×10^5 mol) survey (Table 2).

The change in dissolved methane content in the water column between the surveys is similar to the trend in the number of observed flares and the volume of released gas, and, to a smaller extent, the sea-air methane flux. Although the correlation between the amount of released methane and its content in the water is anticipated, there are number of processes that we did not measure, some of which could alter the methane content in the entire water column, and some, in surface waters alone.

One of these processes is aerobic methane oxidation (MOx), which leads to methane under saturation of deep waters in the entire ocean (Reeburgh, 2007). During MOx, methane is removed from the water column when it is consumed by bacteria who use methane as a source of carbon and energy. To test how important the role of MOx is in the removal of methane from the system, we used MOx rates reported for the regions near our study area. Gentz et al. (2014) reported MOx rate of 0.8 nmol L^{-1} d^{-1} in bottom waters and 0.2 in surface waters in the water column above methane flares with absolute depth of ~250 m, while Steinle et al. (2015) found higher rates of 2 nmol L^{-1} d^{-1} in bottom water alongside lower rates of only 0.1 nmol L^{-1} d^{-1} in surface waters above methane flares with an absolute water depth of 360 m. After vertical and horizontal integration of these estimates over our area, we found that less than 10% of the released methane in our study area per day is likely to be removed from the system through MOx, suggesting that this process does not play a major role in the removal of methane injected from sediments at this site.

Table 2. Average dissolved methane concentrations and content in different layers during each survey

Layer → Survey ↓	Surface (surface-20 m water depth)	Intermediate (variable depth depending on water depth)	Bottom (bottom-15 m above the bottom)	Total
Average methane concentrations (nmol L^{-1})				
June-14	9.4	55.4	92.3	
July-15	3.1	31.9	70	
May-16	3.2	26.6	61.3	
Average content (×10^{-3} mol m^{-2})				
June-14	0.17	3.79	1.39	5.35
July-15	0.06	2.36	1.04	3.46
May-16	0.07	2.32	0.91	3.30
Total content in the surveyed area (×10^5 mol)				
June-14	0.73	16	5.87	23
July-15	0.26	10	4.40	15
May-16	0.28	9.8	3.85	14
Total mass of methane in the surveyed area (t)				
June-14	1.17	25.73	9.41	36.31
July-15	0.43	16.00	7.05	23.50
May-16	0.44	15.77	6.17	22.38

Another process mediating methane content in the water column is aerobic methane production by microbes under phosphorus limiting conditions (Karl et al., 2008). In the oceanic interior, this process leads to methane super saturation in the surface water column above the pycnocline (Reeburgh, 2007). Such methane super saturation in surface waters was found in the Fram Strait to the west from our study area, but only reached maximum concentrations of 9 nM at 10-20 m depth (Damm et al., 2015). We observed only one case of isolated high surface methane concentration (of 20 nmol L^{-1}) during the June-14 and May-16 surveys, but in most cases surface concentrations were close to atmospheric equilibrium, thus we assume that in our study area the methane contribution from this process is of low importance.

These two biological processes are important on the scale of entire ocean but are minor mediators of methane content in our study area, which experiences rapid methane injection into the system at the seabed and methane concentrations hundreds of times higher than the average oceanic concentrations. For example, considering a total injection of methane from sediments of 5.2×10^5 mol d^{-1} (averaged over the three surveys), a loss through sea-air gas exchange of 0.04×10^5 mol d^{-1}, and a MOx rate of 0.58×10^5 mol d^{-1} (based on estimates from Gentz et al. (2014) and Steinle et al. (2015) for nearby waters), the resulting amount of methane in the water column would be 4.6 mol $\times 10^5$ mol d^{-1}. Our total methane content averaged over the three surveys is 17×10^5 mol, which is 3.8 times higher than the resulting content, implying a residence time of methane in the study area of about 3.8 days. However, methane is likely transported beyond our survey area during this time through transport by lateral water movement (section 3.5). To see how efficient this transport is and what affects it in our study area, we look further into vertical and horizontal distribution of methane in different surveys.

3.4 Controls of the vertical distribution of dissolved methane

Highest dissolved methane concentrations were found in the bottom layer (> 300 nmol L^{-1}) in the southwestern part of the sampling area during all three surveys (Figs. 4d-i, 4d-i). Waters supersaturated with methane were found around flares from the seafloor up to 50 (July-15) and 20 meters water depth (June-14, May-16). Methane supersaturated waters have methane concentrations > 3.7 nmol L^{-1}, which would be in equilibrium with the atmosphere for a salinity of 35 at 0° C and atmospheric mole fraction of methane 1.9 ppb (average value for all three surveys) (Wiesenburg and Guinasso, 1979). In all three surveys, the intermediate layer methane concentration averaged over the entire area was only half of the bottom layer concentration, while the surface water concentrations were 25 times lower than the bottom layer concentrations.

Our results show methane enriched bottom and intermediate waters, and surface water which are only slightly supersaturated or close to atmospheric equilibrium. These results agree well with earlier measurements near our study area (e.g. Gentz et al., 2014; Westbrook et al., 2009; Mau et al., 2017), which showed high methane concentrations in bottom waters above methane flares, and rapid decreases in methane concentrations towards the surface. This pattern in vertical distribution can be explained by ongoing gas exchange between rising methane bubbles and the surrounding seawater (e.g. McGinnis et al., 2006). This leads to continuous replacement of methane in the bubbles with N_2 and O_2 from the seawater and methane enrichment of seawater along the bubble ascent. Modelling approaches suggest that the bulk of methane is already stripped out from rising bubbles close to the seafloor, so that bottom waters become more enriched with dissolved methane (McGinnis et al., 2006). Bubbles observed close to the surface are thus mostly comprised of N_2/O_2. Only bubbles of >20 mm in diameter may still contain 1% of their initial methane content at the surface, but such bubbles typically break apart during their ascent (McGinnis et al., 2006).
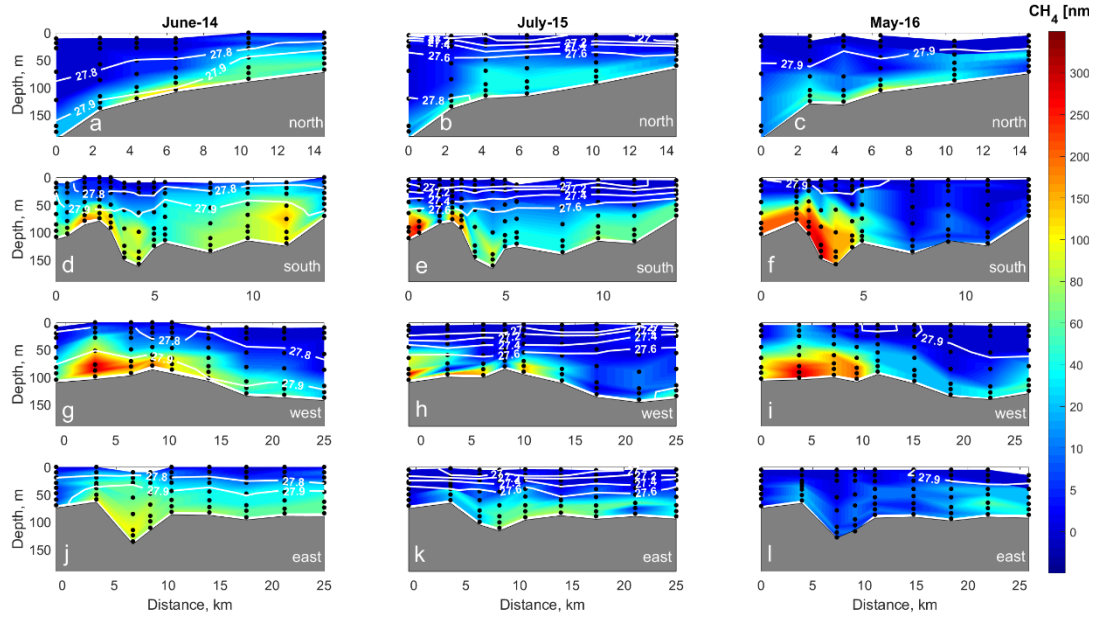
Figure 4. Distribution of dissolved methane along four transects (north (**a**, **c**, **d**), south (**d**, **e**, **f**), west (**g**, **h**, **i**) and east (**j**, **k**, **l**); c.f. Fig. 1 for location and direction of each transect). Seawater density (in kg m^{-3}) is indicated by white contour lines. Locations of discrete samples for methane concentration measurements are indicated by black dots.

Vertical transport of dissolved methane that has already escaped bubbles has been proposed to be limited by water column vertical stratification, when a pycnocline acts as a barrier for vertical mixing of methane rich waters in strongly stratified waters (Gentz et al., 2014; Myhre et al., 2016). As a proxy for water column vertical stratification, we calculated the Brunt–Väisälä frequency (N^2) in our study area (Millard et al., 1990), which generally peaked at ~20m water depth, and was the highest in July-15 (4×10^{-4} s^{-2}), ~8 times lower during the June-14 survey (0.5×10^{-4} s^{-2}) and near zero in the entire water column during the May-16 survey (0.1×10^{-4} s^{-2}) (Fig. 5c). In July-15 the observed strong stratification was formed by a temperature drop from 5.5 °C at the surface to 3.5°C at 50 m water depth forming pronounced thermocline (Fig. 5a); and by a salinity increase from 34.1 at the surface to 34.9 at 100 m depth along a continuous halocline (Fig. 5b). Conversely, in May-16 the water column was well-mixed, with almost uniform temperature and salinity with depth, and the near- absence of a pycnocline.
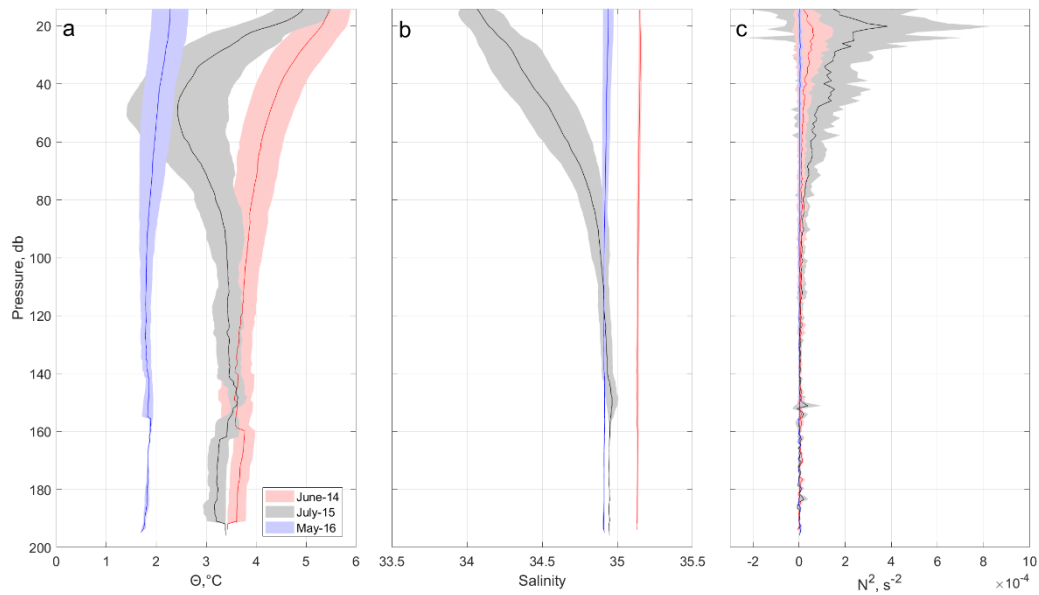
Figure 5. (**a**) Potential temperature (Θ, °C), (**b**) salinity and (**c**) Brunt–Väisälä frequency (N^2, s^{-2}) averaged over all CTD stations for each survey with standard deviation shown as shaded error bars. Colors indicate: June-14 (red), July-15 (black) and May-16 (blue).

Despite the difference in stratification between the three surveys (Fig. 5c), the vertical distribution of dissolved methane (high bottom water methane concentrations and low surface water concentrations) was similar across all three surveys (Fig. 4). This indicates that methane released from the sediments and dissolved in seawater did not rise above 20-50 m water depth towards the sea surface, even in the absence of a pycnocline. Our findings thus suggest that water density stratification may not always play the principle role in the vertical distribution of dissolved methane in cold seeps areas, in contrast to the conclusions of previous studies in this area (Myhre et al., 2016: Gentz et al., 2014). Furthermore, our results do not show an influence of stratification on water column methane content or the sea-air gas flux.

3.5 Controls of horizontal distribution of dissolved methane

The horizontal distribution and patchiness of methane differed between the three surveys. During the June-14 survey, we observed elevated dissolved methane concentrations in the bottom and mid-depth layers (Fig. 6d and g) spread over the entire survey area. In contrast, during May-16, methane concentrations were high (up to 400 nmol L^{-1}) only above flares clustered in the south-western part of the area, and decreased considerably to < 40 nmol L^{-1} within a few hundred meters away from the flares (Fig. 6i). Elevated methane concentrations also spread horizontally in July-15, but to a lesser extent than during the June-14 survey.

In the surface layer, methane concentrations were generally low and near the atmospheric equilibrium (Fig 6a-c). Some elevated surface methane concentrations (~20 nmol L^{-1}) were observed at one station in the southeast part of the study area in June-14 and in the southwestern part of the study area during the May-16 survey.
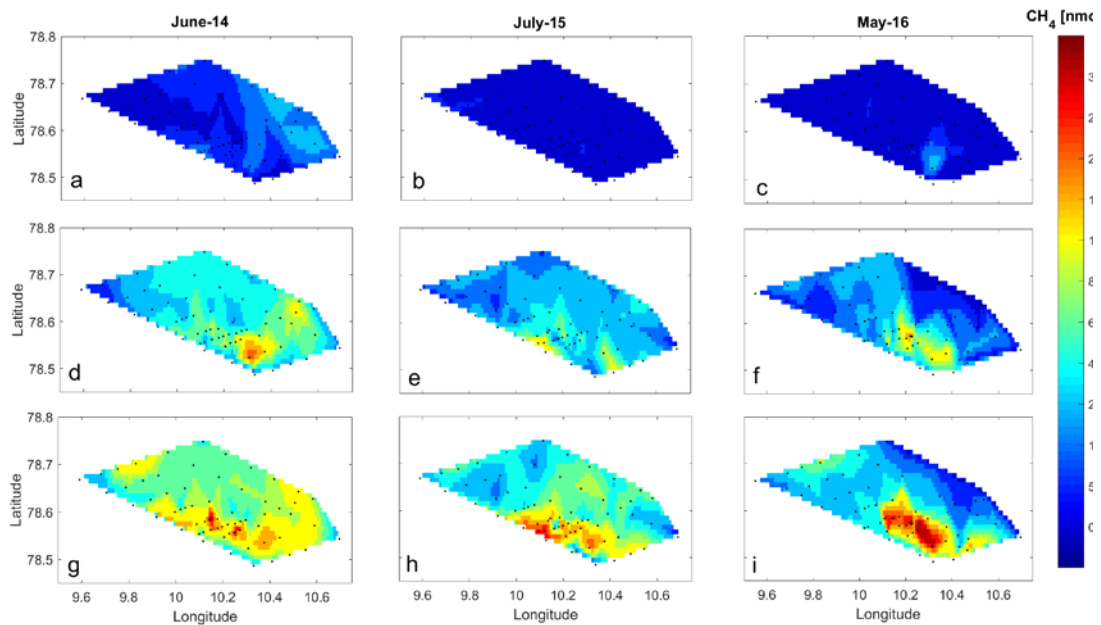
Figure 6. Average methane concentrations in the surface (0-20 m, **a**, **b**, **c**), intermediate (20 m –15 m from the seafloor, **d**, **e**, **f**) and bottom water (within 15 m of the seafloor, **g**, **h**, **i**), layers for the entire grid during the three surveys as indicated above the figures.

High variability in water mass properties indicates that circulation during all surveys was controlled by several factors. We used the classification of water masses suggested by Cottier et al. (2005) for Svalbard fjords and adjacent shelf regions to describe the oceanographic setting in our study area. During the June-14 survey we observed only warm and saline AW (temperature Θ >3°C, absolute salinity S_A >34.65) (Fig. 7a), brought to the study area with the WSC. In contrast, water in July-15 was substantially colder and less saline (Fig. 7b), mainly comprised of AW, with some Transformed Atlantic Water (TAW, $1 < \Theta < 3$°C, S_A >34.65), and to the largest extent, Intermediate Water (IW, Θ >1°C, $34 < S_A < 34.65$). IW originates from fjords and forms as AW that cools over winter in fjords, and is freshened by glacial melt, sea ice melt and river runoff during summer. IW can also be a mix of AW and Arctic Water masses (ArW, $-1.5° < \Theta < 1$°C, $34.3 < S_A < 34.8$) transported from the Northern Barents Sea around southern tip of Svalbard with the ESC. During the May-16 survey (Fig. 7c), the

water column mainly comprised TAW with absolute salinity values similar to AW but with potential temperatures around 1.5 – 3°C, which is colder than the typical AW with temperature defined as above 3°C. There was a strong presence of AW on the shelf and adjacent fjords in 2016 (F. Nilsen, pers. comm.). The core of the AW in May is always above 2.5°C (Beszczynska-Möller et al., 2012). Our measured colder seawater temperatures in the area could indicate that AW was cooled by the atmosphere or surrounding waters, either locally or before it was advected from adjacent basins.
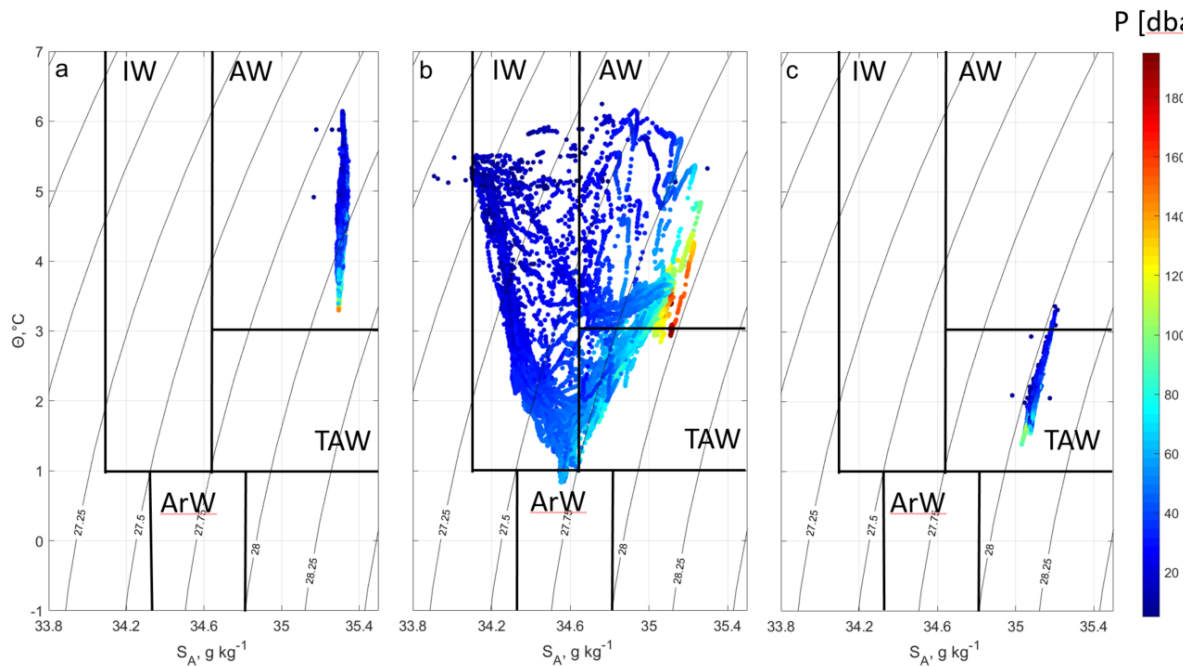
Figure 7. Potential temperature (Θ, °C) – absolute salinity (S_A, g kg^{-1}) diagrams for the June-14 (**a**), July-15 (**b**) and May-16 (**c**) surveys. Θ, °C calculated according to the International Thermodynamic Equation of Seawater (Fofonoff and Millard, 1983). Absolute salinity calculated based on measured practical salinity, and is expressed in terms of g of salt per kg of water. Grey contours indicate isopycnals (kg m^{-3}).

Seawater temperature and salinity modelled with the S800-model (Hattermann et al., 2016) for the study area indicate a shift from AW to IW properties towards summer and autumn months due to surface warming and freshening (Fig. 8), hence revealing the annual cycle of water mass formation. Salinity shows a seasonal cycle only at the surface, where it decreases from 35 in June to 34.4 in September (Fig. 9). Summer freshening of the surface results from freshwater runoff from land, glacial and sea ice melt, and a varying presence of ArW in the study area. Bottom water salinity of about 35 is constant throughout the year, such that the seasonal cycle of density near the seafloor is controlled by temperature. Surface and bottom water temperatures rise towards summer, following atmospheric temperatures, regardless of which water mass is present in the area (Fig. 9). Temperatures increase towards summer from 2.5 to 6°C at the surface, and from 1.5 to 4°C at the bottom. The maximum temperature in the surface water is observed in July-August and one month later near the bottom. Winter surface and bottom temperatures vary between 1.5 and 2.5°C indicating that the water column is cooled down by heat loss to the atmosphere or surrounding waters (Nilsen et al., 2016). Warming of the water column in the study area throughout the year occurs through intermittent heat exchange with

the WSC that floods the shallow shelf (Nilsen et al., 2016), likely in a form of baroclinic eddies, which are abundant in this region (Appen et al., 2016, Hattermann et al., 2016).
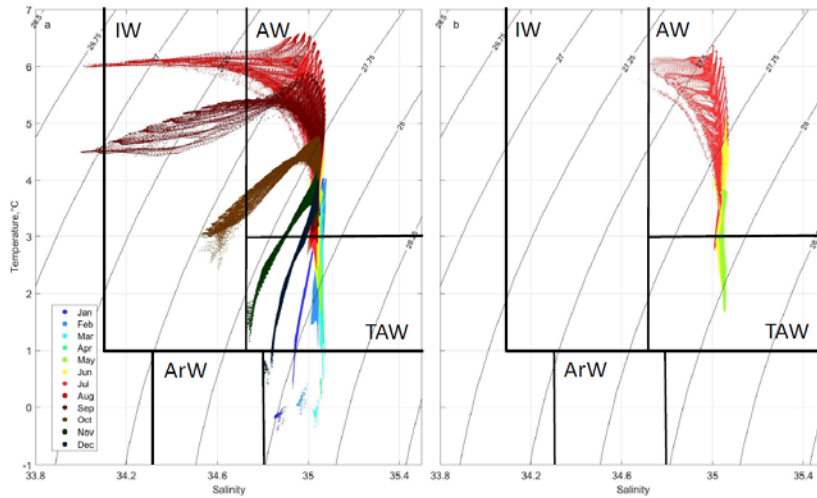

Figure 8. TS diagrams based on S800-model data for the study area, monthly average over the period July 2005 – July 2010 (**a**); monthly average in May, June and July as these months are when the surveys were conducted (**b**). Colors indicate month of the year as shown in the legend. Background contour lines show isopycnals (kg m^{-3}).
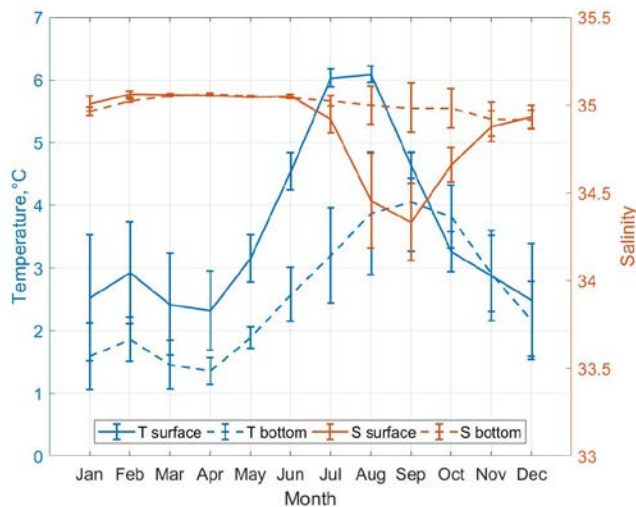
Figure 9. Annual cycle of bottom and surface seawater temperature and salinity in the study area, modelled with S800-model. Lines show mean values for the study area, bars indicate spatial variability.

3.6 Eddy driven seasonal dispersion on the shelf

Our observations indicated a large spatial variability of dissolved methane concentrations, alongside limited vertical penetration of dissolved methane from the sources at the seafloor towards the sea surface irrespective of vertical stratification. Based on this, we propose that lateral advection near the seafloor plays an important role in dispersing methane horizontally away from the seep locations. The

continuous replacement of methane-enriched water with water containing low methane concentrations allows efficient dissolution of methane released in bubbles from the sediments.

As shown on Fig. 6 (g-i), dissolved methane was spread horizontally in the bottom layer during June-14 and July-15 while it was more concentrated around the source in May-16. The water mass analysis suggests that this variability in horizontal dispersion is related to different circulation patterns on the shelf. As previously discussed, circulation of waters on the shallow shelf west of PKF is influenced by the combination of the WSC and superimposed local factors and their seasonality. The sole presence of the AW on the shelf in June-14 for example, which led to high dispersion of dissolved methane above the bottom, can be explained by an AW flooding event from the WSC over the shelf (Nilsen et al., 2008; Nilsen et al., 2016). Thereby, the lateral transport of waters above the PKF shelf during such flooding events disperses the dissolved methane and reduces the residence time of dissolved methane above gas flares.

While the WSC core generally flows further offshore than the shallow PKF shelf (Aagaard et al., 1987), instabilities of the WSC result in formation of numerous eddies that transport AW onto the shallow shelf (Appen et al., 2016, Hattermann et al. 2016, Wekerle et al., 2017). The transport occurs across the slope near the seafloor and plays an important role in the exchange of AW with shelf waters in our study region (Tverberg and Nøst, 2009). We propose that the observed large dispersion of dissolved methane above the bottom during the June-14 survey is a result of eddy activity on the shallow shelf, and that eddies play an important role in the cross-frontal transport of waters and its constituents.

Appen et al. (2016) found increased eddy kinetic energy (EKE) and enhanced baroclinic instability in the WSC in winter and spring and it is likely that this seasonality will affect the number of flooding events over the shallow shelf and the residence time of methane above gas flares. To investigate the relationship between the seasonality of eddy activity and the variability of dissolved methane dispersion on the shelf, we used the S800-model to run numerical experiments releasing and tracking particles simulating methane in our most intense flare area (see Methods 2.5). The particles are freely advected by the three dimensional model velocity field and provide a first order assessment of the role of the circulation in methane dispersion. The buoyancy driven motion of bubbles and the aerobic oxidation of dissolved methane will add further complexity to the dispersion process, but as discussed in section 3.3, are likely to be of secondary importance compared to the advective controls. In the numerical experiment, we observed a clear seasonality in particle dispersion with a much wider area being covered by the particles from January to May as opposed to a limited area of high particle concentrations during the summer months (Fig. 10).

During all months, the particles are mainly advected northward along the shelf and into the Kongsfjorden Trough that crosses the shelf at 79° N. However, in winter and spring, the pattern becomes more dispersive and particles are advected westward off the shelf, suggesting a greater influence of the WSC on water mass exchange with the shallow shelf area. The residence time within our study area follows the seasonal evolution of EKE (Fig 11a), with 50 % (80 %) of the released particles having left the study area after 3 days (6 days) between January to April, when EKE in the study area is largest. Furthermore, particles with the largest displacement (up to 80 – 100 km five days after the release, Fig. 11b) are associated with the highest seawater density of 27.9 – 28.1 kg m^{-3}, which is consistent with the hypothesis that methane is efficiently dispersed by eddies that lift dense AW onto the shelf (Tverberg and Nøst, 2009, Hattermann et al. 2016). Although our observations

during a 3-day period in each year do not resolve the seasonal cycle seen in the model, they support this principal mechanism, with the most dispersed methane concentrations being observed during the June-14 and July-15 surveys when AW was present in the bottom layer. Thus, our combination of observations and modelling suggests that eddies play an important role in dispersing outgassing methane over the continental shelf and in controlling the water column methane content, with potential direct implications for methane related biogeochemical processes.
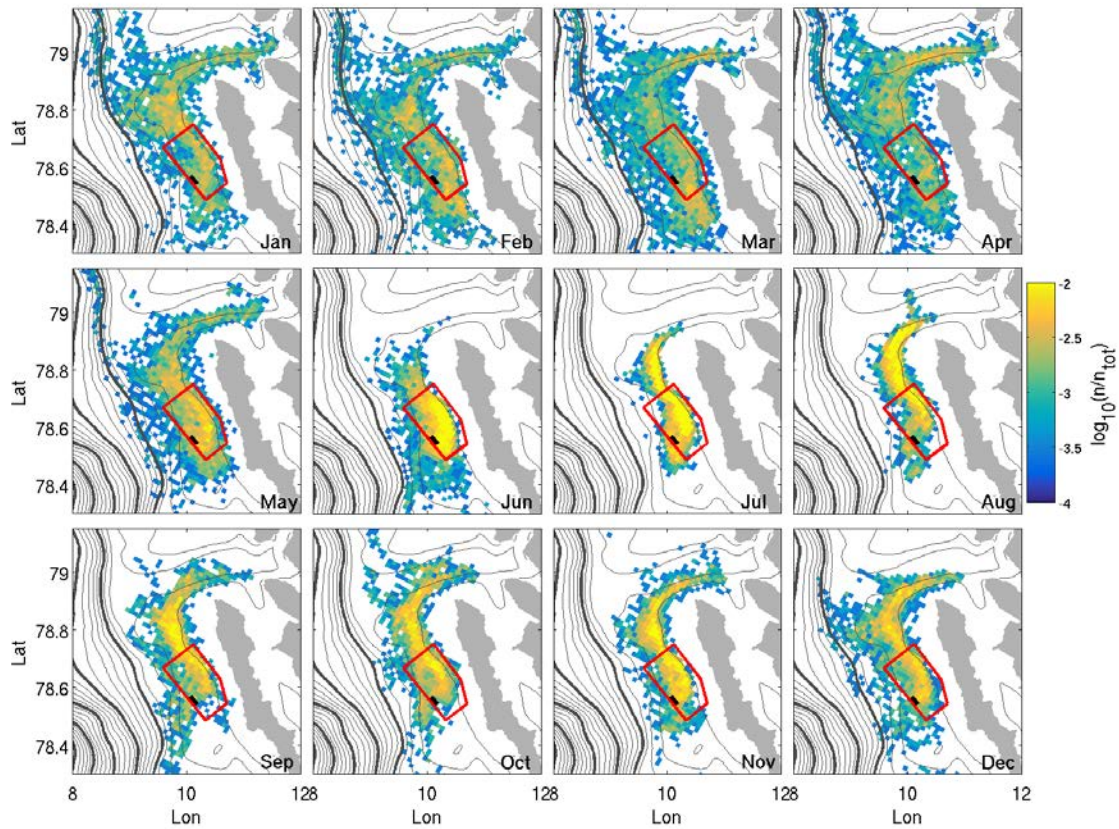
Figure 10. Monthly maps of particle dispersion 5 days after the particle release between 80 and 100 m water depth at the positions indicated by the black rectangle. Colors indicate the number of particles per grid cell normalized by the total number of particles in the respective month, using a logarithmic scale. The red polygon delineates the location of the sampling sites, contours show the isobaths with 100 m intervals thicker lines indicating 500 m intervals.
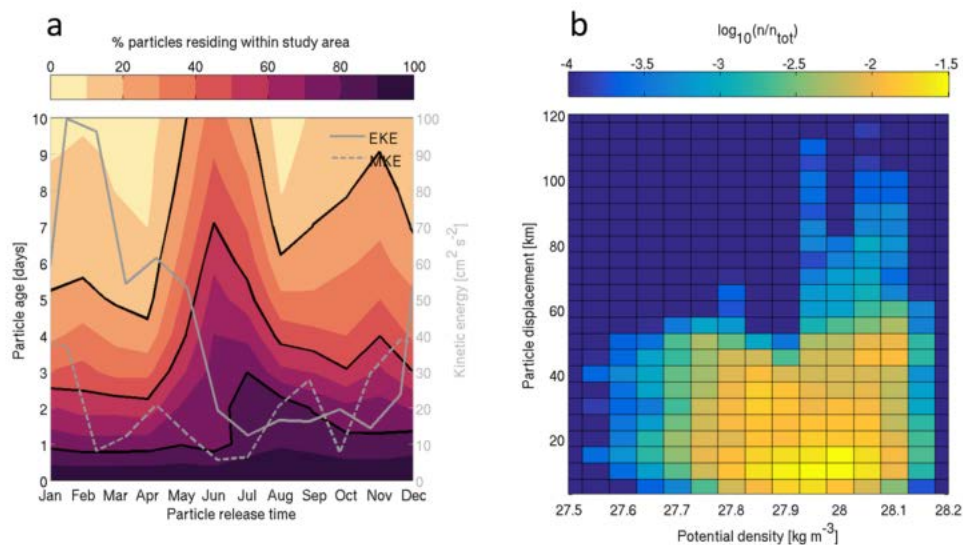
Figure 11. (**a**) Time series showing the residence time of particles within the study area indicated by the red polygon in Fig. 10 (color shade), together with monthly averaged mean- (MKE) and eddy (EKE) kinetic energy (right axis), averaged for the same region. Black curves indicate times when 20 %, 50 % and 80 % of particles have left the study area. (**b**) Two-dimensional histogram of particle displacement vs. potential density at the particle position after five days. Colors indicate the normalized frequency of occurrence on a logarithmic scale, showing that many particles remains within 20 km of the source and that the largest displacements are associated with the highest densities.

4 Conclusions

To our knowledge, this is the first study of the water column above cold methane seeps that combines a series of oceanographic surveys with stations positioned on a grid within a defined polygon. This study clearly benefits from the grid station design when compared to more frequently conducted single synoptic transects. Acquiring data in a four dimensional array in time and space allowed us to fully evaluate the methane content in the entire water body above methane flares and identify the major processes mediating water column methane content and transport.

Our results suggest the possibility of enhanced methane flux from the sediments triggered by elevated bottom water temperature in the absence of underlying gas hydrate. In light of warming waters of the Arctic Ocean, not only gas hydrate containing sediments, but all methane gas bearing sediments could potentially become sources of methane release into the water column. Further study of the processes involved and the links between gas bearing sediments and bottom water temperature is required to improve our understanding.

Comparison between the three different hydrographic regimes observed across the three surveys reveals that most of the released methane in our shallow shelf area remains in the bottom and intermediate waters irrespective of the strength of stratification. Therefore, hypotheses by e.g. von Deimling et al., (2011), who suggested that all methane could be liberated to the atmosphere from shallow shelf areas as a result of a well-mixed water column and absence of stratification appear not to be valid in this shallow shelf study area. Small amounts of methane could be liberated to the

atmosphere, but mainly as a result of strong winds increasing the rate of air-sea gas exchange, not weak stratification.

Instead of vertical transport processes, we find that horizontal advection is the main mechanism that controls the dispersion of dissolved methane on the Prins Karls Forland shelf. In particular, our results highlight the role of mesoscale eddies in controlling the methane content above, dispersion around, and displacement away from gas flares. This implies that eddies and horizontal dispersion may also have important effects on methane related biogeochemical process and the magnitude of different methane sinks. For example, one could anticipate that a potential for methane sink through MOx could be higher when eddy activity is high in winter and spring season, because by dispersing dissolved methane over a larger area, eddies promote delivery of dissolved methane to methane oxidizing bacteria that consequently capture and consume this methane. Further seasonal measurements and/or process oriented modelling will be required to scrutinize these ideas, but these results could considerably shift our understanding of the seasonality of sinks of dissolved methane and allow better estimates of the balance between amounts of methane released from sediments, methane liberated into the atmosphere, and methane removed from the system through microbial processes.

Acknowledgements

References

Aagaard, K., Foldvik, A., & Hillman, S. (1987). The West Spitsbergen Current: disposition and water mass transformation. Journal of Geophysical Research: Oceans, 92(C4), 3778-3784.

Albretsen, J., Hattermann, T., & Sundfjord, A. (2017). Ocean and sea ice circulation model results from Svalbard area (ROMS) [Data set]. Norwegian Polar Institute.

Amante, C. (2009). ETOPO1 1 arc-minute global relief model: procedures, data sources and analysis. http://www. ngdc. noaa. gov/mgg/global/global. html.

Andreassen, K., Hubbard, A., Winsborrow, M., Patton, H., Vadakkepuliyambatta, S., Plaza-Faverola, A., . . . Mattingsdal, R. (2017). Massive blow-out craters formed by hydrate-controlled methane expulsion from the Arctic seafloor. Science, 356(6341), 948-953.

Appen, W.-J. v., Schauer, U., Hattermann, T., & Beszczynska-Möller, A. (2016). Seasonal cycle of mesoscale instability of the West Spitsbergen Current. Journal of Physical Oceanography, 46(4), 1231-1254.

Berge, J., Johnsen, G., Nilsen, F., Gulliksen, B., & Slagstad, D. (2005). Ocean temperature oscillations enable reappearance of blue mussels Mytilus edulis in Svalbard after a 1000 year absence. Marine Ecology Progress Series, 303, 167-175.

Berndt, C., Feseker, T., Treude, T., Krastel, S., Liebetrau, V., Niemann, H., . . . Ferré, B. (2014). Temporal constraints on hydrate-controlled methane seepage off Svalbard. Science, 343(6168), 284-287.

Beszczynska-Möller, A., Fahrbach, E., Schauer, U., & Hansen, E. (2012). Variability in Atlantic water temperature and transport at the entrance to the Arctic Ocean, 1997–2010. ICES Journal of Marine Science, 69(5), 852-863.

Budgell, W. (2005). Numerical simulation of ice-ocean variability in the Barents Sea region. Ocean Dynamics, 55(3-4), 370-387.

Cottier, F., Nilsen, F., Inall, M., Gerland, S., Tverberg, V., & Svendsen, H. (2007). Wintertime warming of an Arctic shelf in response to large-scale atmospheric circulation. Geophysical Research Letters, 34(10).

Cottier, F., Tverberg, V., Inall, M., Svendsen, H., Nilsen, F., & Griffiths, C. (2005). Water mass modification in an Arctic fjord through cross-shelf exchange: The seasonal hydrography of Kongsfjorden, Svalbard. Journal of Geophysical Research: Oceans, 110(C12).

Cottier, F. R., Nilsen, F., Skogseth, R., Tverberg, V., Skarðhamar, J., & Svendsen, H. (2010). Arctic fjords: a review of the oceanographic environment and dominant physical processes. Geological Society, London, Special Publications, 344(1), 35-50.

Crews, L., Sundfjord, A., Albretsen, J., & Hattermann, T. (2018). Mesoscale eddy activity and transport in the Atlantic Water inflow region north of Svalbard. Journal of Geophysical Research: Oceans, 123(1), 201-215.

Damm, E., Mackensen, A., Budéus, G., Faber, E., & Hanfland, C. (2005). Pathways of methane in seawater: Plume spreading in an Arctic shelf environment (SW-Spitsbergen). Continental Shelf Research, 25(12), 1453-1472.

Damm, E., Thoms, S., Beszczynska-Möller, A., Nöthig, E.-M., & Kattner, G. (2015). Methane excess production in oxygen-rich polar water and a model of cellular conditions for this paradox. Polar Science, 9(3), 327-334.

Dee, D. P., Uppala, S., Simmons, A., Berrisford, P., Poli, P., Kobayashi, S., . . . Bauer, P. (2011). The ERA-Interim reanalysis: Configuration and performance of the data assimilation system. Quarterly Journal of the royal meteorological society, 137(656), 553-597.

Döös, K., Jönsson, B., & Kjellsson, J. (2017). Evaluation of oceanic and atmospheric trajectory schemes in the TRACMASS trajectory model v6. 0. Geoscientific Model Development, 10(4), 1733.

Ferré, B., Mienert, J., & Feseker, T. (2012). Ocean temperature variability for the past 60 years on the Norwegian-Svalbard margin influences gas hydrate stability on human time scales. Journal of Geophysical Research: Oceans, 117(C10).

Fofonoff, N. P., & Millard Jr, R. (1983). Algorithms for the computation of fundamental properties of seawater.

Gentz, T., Damm, E., von Deimling, J. S., Mau, S., McGinnis, D. F., & Schlüter, M. (2014). A water column study of methane around gas flares located at the West Spitsbergen continental margin. Continental Shelf Research, 72, 107-118.

Graversen, R. G., Mauritsen, T., Tjernström, M., Källén, E., & Svensson, G. (2008). Vertical structure of recent Arctic warming. Nature, 451(7174), 53.

Graves, C. A., Steinle, L., Rehder, G., Niemann, H., Connelly, D. P., Lowry, D., . . . James, R. H. (2015). Fluxes and fate of dissolved methane released at the seafloor at the landward limit of the gas hydrate stability zone offshore western Svalbard. Journal of Geophysical Research: Oceans, 120(9), 6185-6201.

Greinert, J., Artemov, Y., Egorov, V., De Batist, M., & McGinnis, D. (2006). 1300-m-high rising bubbles from mud volcanoes at 2080 m in the Black Sea: Hydroacoustic characteristics and temporal variability. Earth and Planetary Science Letters, 244(1-2), 1-15.

Hanson, R. S., & Hanson, T. E. (1996). Methanotrophic bacteria. Microbiological reviews, 60(2), 439-471.

Hattermann, T., Isachsen, P. E., Appen, W. J., Albretsen, J., & Sundfjord, A. (2016). Eddy-driven recirculation of Atlantic Water in Fram Strait. Geophysical Research Letters, 43(7), 3406-3414.

Hester, K. C., & Brewer, P. G. (2009). Clathrate hydrates in nature. Annual review of marine science, 1, 303-327.

Hsu, S., Meindl, E. A., & Gilhousen, D. B. (1994). Determining the power-law wind-profile exponent under near-neutral stability conditions at sea. Journal of Applied Meteorology, 33(6), 757-765.

Jakobsson, M., Mayer, L., Coakley, B., Dowdeswell, J. A., Forbes, S., Fridman, B., . . . Rebesco, M. (2012). The international bathymetric chart of the Arctic Ocean (IBCAO) version 3.0. Geophysical Research Letters, 39(12).

James, R. H., Bousquet, P., Bussmann, I., Haeckel, M., Kipfer, R., Leifer, I., . . . Rehder, G. (2016). Effects of climate change on methane emissions from seafloor sediments in the Arctic Ocean: A review. Limnology and Oceanography, 61(S1).

Kannberg, P. K., Tréhu, A. M., Pierce, S. D., Paull, C. K., & Caress, D. W. (2013). Temporal variation of methane flares in the ocean above Hydrate Ridge, Oregon. Earth and Planetary Science Letters, 368, 33-42.

Karl, D. M., Beversdorf, L., Björkman, K. M., Church, M. J., Martinez, A., & Delong, E. F. (2008). Aerobic production of methane in the sea. Nature Geoscience, 1(7), 473.

Kessler, J. D., Valentine, D. L., Redmond, M. C., Du, M., Chan, E. W., Mendes, S. D., . . . Werra, L. M. (2011). A persistent oxygen anomaly reveals the fate of spilled methane in the deep Gulf of Mexico. Science, 331(6015), 312-315.

Knies, J., Damm, E., Gutt, J., Mann, U., & Pinturier, L. (2004). Near-surface hydrocarbon anomalies in shelf sediments off Spitsbergen: Evidences for past seepages. Geochemistry, Geophysics, Geosystems, 5(6).

Kort, E., Wofsy, S., Daube, B., Diao, M., Elkins, J., Gao, R., . . . Moore, F. (2012). Atmospheric observations of Arctic Ocean methane emissions up to 82 north. Nature Geoscience, 5(5), 318.

Kretschmer, K., Biastoch, A., Rüpke, L., & Burwicz, E. (2015). Modeling the fate of methane hydrates under global warming. Global Biogeochemical Cycles, 29(5), 610-625.

Kvenvolden, K. A., Lilley, M. D., Lorenson, T. D., Barnes, P. W., & McLaughlin, E. (1993). The Beaufort Sea continental shelf as a seasonal source of atmospheric methane. Geophysical Research Letters, 20(22), 2459-2462.

Lammers, S., Suess, E., & Hovland, M. (1995). A large methane plume east of Bear Island (Barents Sea): implications for the marine methane cycle. Geologische Rundschau, 84(1), 59-66.

LANDVIK, J. Y., Ingolfsson, O., MIENERT, J., LEHMAN, S. J., Solheim, A., ELVERHØI, A., & Ottesen, D. (2005). Rethinking Late Weichselian ice-sheet dynamics in coastal NW Svalbard. Boreas, 34(1), 7-24.

Leifer, I., Jeuthe, H., Gjøsund, S. H., & Johansen, V. (2009). Engineered and natural marine seep, bubble-driven buoyancy flows. Journal of Physical Oceanography, 39(12), 3071-3090.

Marín-Moreno, H., Minshull, T. A., Westbrook, G. K., & Sinha, B. (2015). Estimates of future warming-induced methane emissions from hydrate offshore west Svalbard for a range of climate models. Geochemistry, Geophysics, Geosystems, 16(5), 1307-1323.

Mau, S., Römer, M., Torres, M. E., Bussmann, I., Pape, T., Damm, E., . . . Loher, M. (2017). Widespread methane seepage along the continental margin off Svalbard-from Bjørnøya to Kongsfjorden. Scientific reports, 7, 42997.

McGinnis, D. F., Greinert, J., Artemov, Y., Beaubien, S., & Wüest, A. (2006). Fate of rising methane bubbles in stratified waters: How much methane reaches the atmosphere? Journal of Geophysical Research: Oceans, 111(C9).

Millard, R., Owens, W., & Fofonoff, N. (1990). On the calculation of the Brunt-Väisälä frequency. Deep Sea Research Part A. Oceanographic Research Papers, 37(1), 167-181.

Myhre, C. L., Ferré, B., Platt, S. M., Silyakova, A., Hermansen, O., Allen, G., . . . Pitt, J. (2016). Extensive release of methane from Arctic seabed west of Svalbard during summer 2014 does not influence the atmosphere. Geophysical Research Letters, 43(9), 4624-4631.

Nikolovska, A., Sahling, H., & Bohrmann, G. (2008). Hydroacoustic methodology for detection, localization, and quantification of gas bubbles rising from the seafloor at gas seeps from the eastern Black Sea. Geochemistry, Geophysics, Geosystems, 9(10).

Nilsen, F., Cottier, F., Skogseth, R., & Mattsson, S. (2008). Fjord–shelf exchanges controlled by ice and brine production: the interannual variation of Atlantic Water in Isfjorden, Svalbard. Continental Shelf Research, 28(14), 1838-1853.

Nilsen, F., Skogseth, R., Vaardal-Lunde, J., & Inall, M. (2016). A simple shelf circulation model: Intrusion of Atlantic water on the West Spitsbergen shelf. Journal of Physical Oceanography, 46(4), 1209-1230.

Ostrovsky, I., McGinnis, D. F., Lapidus, L., & Eckert, W. (2008). Quantifying gas ebullition with echosounder: the role of methane transport by bubbles in a medium-sized lake. Limnology and Oceanography: Methods, 6(2), 105-118.

Parmentier, F.-J. W., Silyakova, A., Biastoch, A., Kretschmer, K., & Panieri, G. (2015). Natural marine methane sources in the Arctic. In: Arctic Monitoring and Assessment Programme (AMAP).

Paull, C. K., Ussler, W., Dallimore, S. R., Blasco, S. M., Lorenson, T. D., Melling, H., . . . McLaughlin, F. A. (2007). Origin of pingo-like features on the Beaufort Sea shelf and their possible relationship to decomposing methane gas hydrates. Geophysical Research Letters, 34(1).

Perkin, R., & Lewis, E. (1984). Mixing in the West Spitsbergen current. Journal of Physical Oceanography, 14(8), 1315-1325.

Pierrot, D., Neill, C., Sullivan, K., Castle, R., Wanninkhof, R., Lüger, H., . . . Cosca, C. E. (2009). Recommendations for autonomous underway pCO2 measuring systems and data-reduction routines. Deep Sea Research Part II: Topical Studies in Oceanography, 56(8-10), 512-522.

Polyakov, I., Alekseev, G., Timokhov, L., Bhatt, U., Colony, R., Simmons, H., . . . Zakharov, V. (2004). Variability of the intermediate Atlantic water of the Arctic Ocean over the last 100 years. Journal of Climate, 17(23), 4485-4497.

Polyakov, I., Timokhov, L., Dmitrenko, I., Ivanov, V., Simmons, H., Beszczynska-Möller, A., . . . Gascard, J. C. (2007). Observational program tracks Arctic Ocean transition to a warmer state. Eos, Transactions American Geophysical Union, 88(40), 398-399.

Polyakov, I. V., Timokhov, L. A., Alexeev, V. A., Bacon, S., Dmitrenko, I. A., Fortier, L., . . . Ivanov, V. V. (2010). Arctic Ocean warming contributes to reduced polar ice cap. Journal of Physical Oceanography, 40(12), 2743-2756.

Portnov, A., Smith, A. J., Mienert, J., Cherkashov, G., Rekant, P., Semenov, P., . . . Vanshtein, B. (2013). Offshore permafrost decay and massive seabed methane escape in water depths> 20 m at the South Kara Sea shelf. Geophysical Research Letters, 40(15), 3962-3967.

Portnov, A., Vadakkepuliyambatta, S., Mienert, J., & Hubbard, A. (2016). Ice-sheet-driven methane storage and release in the Arctic. Nature communications, 7, 10314.

Reeburgh, W. S. (2007). Oceanic methane biogeochemistry. Chemical reviews, 107(2), 486-513.

Römer, M., Riedel, M., Scherwath, M., Heesemann, M., & Spence, G. D. (2016). Tidally controlled gas bubble emissions: A comprehensive study using long-term monitoring data from the NEPTUNE cabled observatory offshore Vancouver Island. Geochemistry, Geophysics, Geosystems, 17(9), 3797-3814.

Rudels, B., Jones, E., Anderson, L., & Kattner, G. (1994). On the intermediate depth waters of the Arctic Ocean. The polar oceans and their role in shaping the global environment, 33-46.

Sahling, H., Römer, M., Pape, T., Bergès, B., dos Santos Fereirra, C., Boelmann, J., . . . Dimmler, W. (2014). Gas emissions at the continental margin west of Svalbard: mapping, sampling, and quantification. Biogeosciences, 11(21), 6029.

Sarkar, S., Berndt, C., Minshull, T. A., Westbrook, G. K., Klaeschen, D., Masson, D. G., . . . Thatcher, K. E. (2012). Seismic evidence for shallow gas-escape features associated with a retreating gas hydrate zone offshore west Svalbard. Journal of Geophysical Research: Solid Earth, 117(B9).

Schmale, O., Greinert, J., & Rehder, G. (2005). Methane emission from high-intensity marine gas seeps in the Black Sea into the atmosphere. Geophysical Research Letters, 32(7).

Serov, P., Portnov, A., Mienert, J., Semenov, P., & Ilatovskaya, P. (2015). Methane release from pingo-like features across the South Kara Sea shelf, an area of thawing offshore permafrost. Journal of Geophysical Research: Earth Surface, 120(8), 1515-1529.

Serov, P., Vadakkepuliyambatta, S., Mienert, J., Patton, H., Portnov, A., Silyakova, A., . . . Andreassen, K. (2017). Postglacial response of Arctic Ocean gas hydrates to climatic amelioration. Proceedings of the National Academy of Sciences, 201619288.

Serreze, M. C., & Francis, J. A. (2006). The Arctic amplification debate. Climatic change, 76(3-4), 241-264.

Shakhova, N., Semiletov, I., Leifer, I., Sergienko, V., Salyuk, A., Kosmach, D., . . . Tumskoy, V. (2013). Ebullition and storm-induced methane release from the East Siberian Arctic Shelf. Nature Geoscience, 7(1), ngeo2007.

Shakhova, N., Semiletov, I., Salyuk, A., Yusupov, V., Kosmach, D., & Gustafsson, Ö. (2010). Extensive methane venting to the atmosphere from sediments of the East Siberian Arctic Shelf. Science, 327(5970), 1246-1250.

Shchepetkin, A. F., & McWilliams, J. C. (2005). The regional oceanic modeling system (ROMS): a split-explicit, free-surface, topography-following-coordinate oceanic model. Ocean modelling, 9(4), 347-404.

Smith, A. J., Mienert, J., Bünz, S., & Greinert, J. (2014). Thermogenic methane injection via bubble transport into the upper Arctic Ocean from the hydrate-charged Vestnesa Ridge, Svalbard. Geochemistry, Geophysics, Geosystems, 15(5), 1945-1959.

Soreide, N. N., Jeffries, M., Richter-Menge, J., & Overland, J. (2016). The Arctic Report Card. Bulletin of the American Meteorological Society, 97(8), 1339-1341.

Steinle, L., Graves, C. A., Treude, T., Ferré, B., Biastoch, A., Bussmann, I., . . . Behrens, E. (2015). Water column methanotrophy controlled by a rapid oceanographic switch. Nature Geoscience, 8(5), 378.

Storkey, D., Blockley, E., Furner, R., Guiavarc'h, C., Lea, D., Martin, M., . . . Siddorn, J. (2010). Forecasting the ocean state using NEMO: The new FOAM system. Journal of operational oceanography, 3(1), 3-15.

Teigen, S. H., Nilsen, F., & Gjevik, B. (2010). Barotropic instability in the West Spitsbergen Current. Journal of Geophysical Research: Oceans, 115(C7).

Tverberg, V., & Nøst, O. (2009). Eddy overturning across a shelf edge front: Kongsfjorden, west Spitsbergen. Journal of Geophysical Research: Oceans, 114(C4).

Veloso, M., Greinert, J., Mienert, J., & De Batist, M. (2015). A new methodology for quantifying bubble flow rates in deep water using splitbeam echosounders: Examples from the Arctic offshore NW-Svalbard. Limnology and Oceanography: Methods, 13(6), 267-287.

von Deimling, J. S., Rehder, G., Greinert, J., McGinnnis, D., Boetius, A., & Linke, P. (2011). Quantification of seep-related methane gas emissions at Tommeliten, North Sea. Continental Shelf Research, 31(7-8), 867-878.

Wallmann, K., Riedel, M., Hong, W., Patton, H., Hubbard, A., Pape, T., . . . Torres, M. (2018). Gas hydrate dissociation off Svalbard induced by isostatic rebound rather than global warming. Nature communications, 9(1), 83.

Wanninkhof, R., Asher, W. E., Ho, D. T., Sweeney, C., & McGillis, W. R. (2009). Advances in quantifying air-sea gas exchange and environmental forcing.

Weiss, R., & Price, B. (1980). Nitrous oxide solubility in water and seawater. Marine chemistry, 8(4), 347-359.

Wekerle, C., Wang, Q., von Appen, W. J., Danilov, S., Schourup-Kristensen, V., & Jung, T. (2017). Eddy-Resolving Simulation of the Atlantic Water Circulation in the Fram Strait With Focus on the Seasonal Cycle. Journal of Geophysical Research: Oceans, 122(11), 8385-8405.

Westbrook, G. K., Thatcher, K. E., Rohling, E. J., Piotrowski, A. M., Pälike, H., Osborne, A. H., . . . James, R. H. (2009). Escape of methane gas from the seabed along the West Spitsbergen continental margin. Geophysical Research Letters, 36(15).

Wiesenburg, D. A., & Guinasso Jr, N. L. (1979). Equilibrium solubilities of methane, carbon monoxide, and hydrogen in water and sea water. Journal of Chemical and Engineering Data, 24(4), 356-360.

Physical controls of dynamics of methane venting from a shallow seep area west of Svalbard

A. Silyakova[1], P. Jansson[1], P. Serov[1], B. Ferré[1], A. K. Pavlov[2], T. Hattermann[3,4], C. A. Graves[5,6], S. M. Platt[7], C. Lund Myhre[7], F. Gründger[1] and H. Niemann[8,1,9]

[1]CAGE-Centre for Arctic Gas Hydrate, Environment and Climate, UiT the Arctic University of Norway in Tromsø, Department of Geosciences, Tromsø, Norway

[2]Norwegian Polar Institute, Fram Centre, Tromsø, Norway

[3]Akvaplan-niva AS, Fram Centre, Tromsø, Norway

[4]Alfred Wegener Institute, Helmholtz Centre for Polar and Marine Research, Bremerhaven, Germany

[5]Leibniz Institute for Baltic Sea Research Warnemünde, Rostock, Germany

[6]Centre for Environment, Fisheries and Aquaculture Science, Lowestoft, UK

[7]NILU - Norwegian Institute for Air Research, Kjeller, Norway

[8]University of Basel, Basel, Switzerland

[9]NIOZ Royal Netherlands Institute for Sea Research, Department of Marine Microbiology & Biogeochemistry, the Netherlands

Contents of this file

Text S1 to S2, Figures S1 to S3

Introduction

Supporting Text S1 and Figure S1 provide details of the method of scaling up gas flow rate estimates to the entire study area.

Supporting Text S2 and Figure S2 provide a detailed description of the water column methane content calculations in different layers.

Supporting Figure S3 shows additional information on bottom water temperature to support the main text in Results and Discussion section 3.1.

Text S1. Method for scaling up the flow rates

Because the fraction of the study area covered by the echosounder was small and slightly different between the three surveys, we applied a scaling up procedure including a Kriging interpolation to facilitate comparison between surveys (Figure S1). The entire area was gridded into cells of 100×100 m, and, as a result three types of cells were considered: 1) completely covered, 2) partly covered or 3) not covered by the echosounder beam footprint. For each cell, we estimated methane flow rates: (a) If one or several flares were detected within cell type 1, the estimated flow rate was applied for the entire cell area. (b) In the absence of flares in cell type 1, the flow rate was set to zero. (c) If one or several flares were within cell type 2, the sum of the flow rates within the cell was normalized by the fraction of the cell covered by the beam footprint. (d) In the absence of flares in cell type 2, the flow rate was set to zero. (e) For cell type 3, (no data acquired) we interpolated flow rates from neighbouring cells. In order to find a smooth and plausible flowrate distribution, a 3x3 low-pass filter, and the Kriging interpolation method embedded in ArcGIS was applied. Finally, to calculate the mean flux (mol m^{-2} s^{-1}) in the entire area, the sum of the scaled up flow rates were normalized by the survey area (Table 1).

Text S2. Calculation of methane content in the water column

Methane content in the water column was calculated by integrating distinct methane concentration values over depth. For this approach, we approximated the definite integral linearly by applying the trapezoid rule. For each discrete sampling point shown on Fig. S2, we had a corresponding depth (Z, m) and CH_4 concentration (C, nmol L^{-1}). To determine the vertically integrated methane content (C_{int}) for every depth (meter) of water column between sampling points (nmol L^{-1} m) we interpolated linearly as follows:

$$C_{int}=(CS_1+CS_2)/2*(ZS_2-ZS_1) \qquad \text{(Eq. SI1)}$$

We then summed all C_{int} in each layer and multiplied by 10^3 to obtain methane content per m^2 in every layer (nmol m^{-2}) for each of the CTD stations.

To account for spatial sampling irregularity between CTD stations, we determined the area-weighted average of the CH_4 content for each layer. For this, we created a grid between longitudes 9.5° E and 10.8° E and latitudes 78.4° N and 78.7° N with bin sizes of $0.01 \times 0.01°$ in both directions. The resulting grid included 101×201 points. We then projected C_{int} for each layer and station onto this grid using the Matlab function griddata for horizontal interpolation. Finally, we calculated the area-weighted average using the Matlab function mean2 of the gridded data. Then we scaled up (multiplied) the area-weighted averages for each layer to the size of the investigated area (423 km^2), yielding the total methane content (in mol) for each layer.
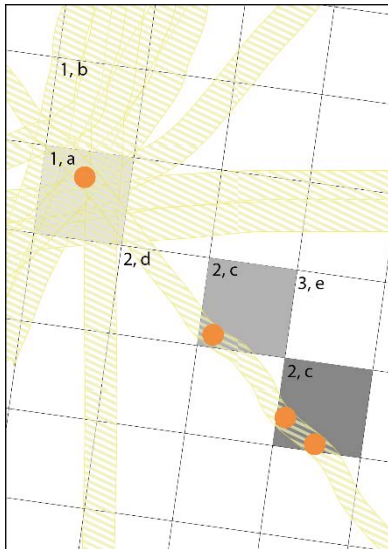
Figure S1. Schematic of flowrate interpolation. Squares indicate 100x100 meter grid cells where the darkness indicates the relative summed flow rates within each cell. Yellow-hashed areas indicate the echosounder beam coverage and dots indicate flares. Cell types 1 – 3 and interpolation schemes a – e are described in the text S1.
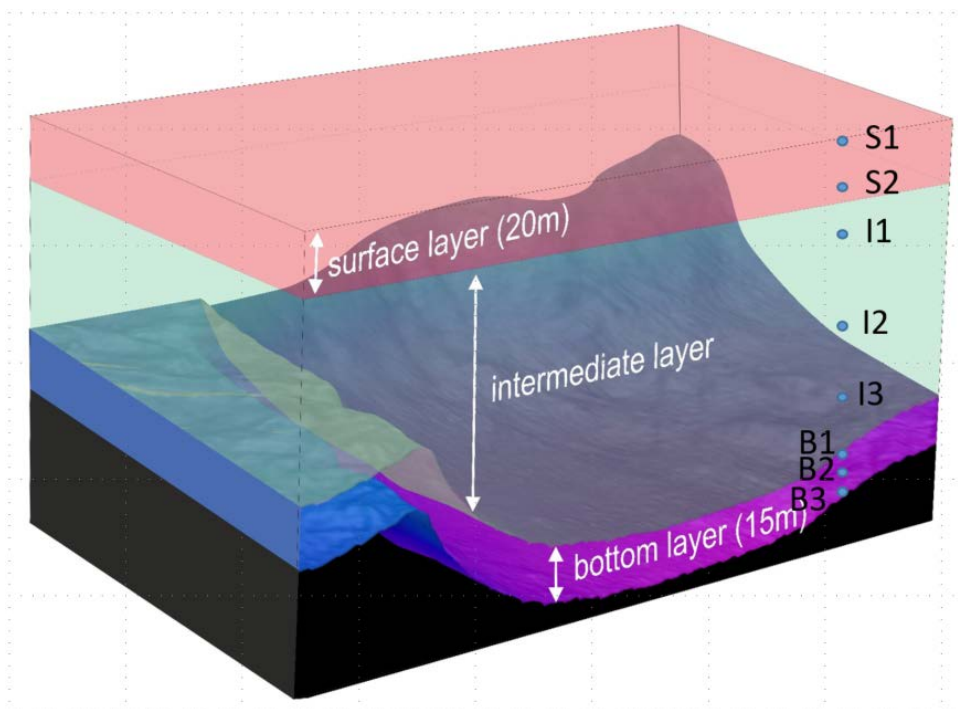

Figure S2. Schematic shows the bottom layer (0-15 meters above seafloor), the intermediate layer (15 meters above seafloor to 20 m water depth) and the surface layer (20 m water depth to sea surface). The blue dots show discrete sampling points in the surface (S1, S2), intermediate (I1, I2, I3) and bottom (B1, B2, B3) layer.
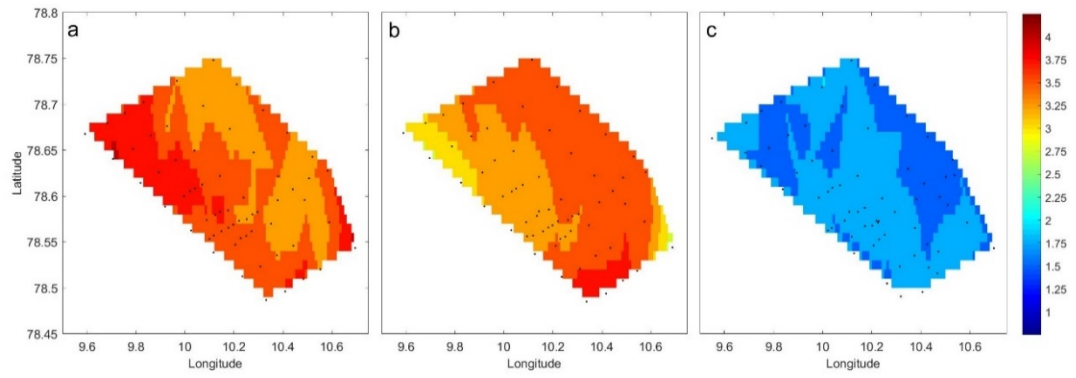
Figure S3. Bottom water temperature during the June-14 (**a**), July-15 (**b**) and May-16 (**c**) surveys.